



Cu nanocrystals coupled with poly (heptazine imide) for synergistically enhanced photocatalytic CH₃SH elimination: Facet engineering strengthened electron pump effect

Tao Zhong^a, Su Tang^a, Wenbin Huang^a, Wei Liu^a, Huinan Zhao^{a,*}, Lingling Hu^a,
Shuanghong Tian^{a,b}, Chun He^{a,b,**,1}

^a School of Environmental Science and Engineering, Sun Yat-sen University, Guangzhou 510275, China

^b Guangdong Provincial Key Laboratory of Environmental Pollution Control and Remediation Technology, Guangzhou 510275, China

ARTICLE INFO

Keywords:

Cu Nanocrystals
Facet engineering
Electron pump effect
Charge transfer
CH₃SH elimination

ABSTRACT

The efficient separation and utilization of intrinsic carriers in photocatalyst, as well as the adsorption and elimination of target pollutants, are two critical challenges in the development of photocatalytic oxidation technology. Herein, the different crystal facet of Cu (111), Cu (100), Cu (111 +100) were engineered and coupled with Poly (heptazine imide) (PHI) as an emerging photocatalyst for CH₃SH elimination under simulated solar light (SSL). Cu (111)/PHI exhibited 87.8% elimination efficiency after 30 min of illumination, significantly higher than that of pure PHI (60.4%), Cu (100)/PHI (71.5%), and Cu (111 +100)/PHI (70.4%). Besides, the photocatalytic performance was maintained at 83.3% after a prolonged reaction time of up to 450 min, indicating that Cu (111)/PHI has good stability and reusability. A comprehensive characterizations study confirmed that Cu (111) exhibited the enhanced surface electron pump effect compared to Cu (100) and Cu (111 +100), facilitating the accelerated extraction and transfer of photogenerated charge carriers. Density functional theory (DFT) calculations revealed that Cu (111) surface active sites can effectively adsorb H₂O, O₂, and CH₃SH due to unsaturated pairing of d-orbital electrons, thus prompting the activation of H₂O, O₂ into reactive oxygen species ($\bullet\text{OH}/\bullet\text{O}_2^-/\text{O}_2$) for the eliminating of adjacent CH₃SH. This study presents a new facet engineering approach for the rational design of highly efficient photocatalysts for the elimination of S-VOCs.

1. Introduction

The extensive emission of volatile organic compounds (VOCs) in daily activities have resulted in the generation of toxic secondary pollutants, such as acid rain, haze, and ozone, posing a grave threat to human health [1]. Especially, sulfur-containing VOCs (S-VOCs), as a characteristic pollutant, have gained attention from researchers due to their malodor, high toxicity, and low environmental thresholds [2]. Therefore, there is an urgent need to develop efficient and sustainable green technologies to eliminate S-VOCs. Among the various green technologies, photocatalytic oxidation (PCO) has emerged as a promising strategy, which can operate under mild and controlled environmental conditions, and effectively convert S-VOCs into non-toxic substances [3]. Recently, a series of semiconductor based photocatalysts

were demonstrated to have excellent S-VOC elimination activities, like CeO₂, BiOX (X = Cl, Br, I), In₂O₃, WO₃, and MnO₂ etc. [4,5]. Nevertheless, the drawbacks of the low photogenerated electrons mobility and the inability to activate the absorbed S-VOC molecules have led to inefficient elimination of S-VOC by PCO technology. Therefore, the design of highly active photocatalysts were necessary to achieve highly efficient elimination of CH₃SH.

Poly (heptazine imide) (PHI) is a recently studied photocatalyst that has a more extensive π -conjugation system, well-defined band gap structures ($E_g \approx 2.70$ eV), robust stability and enriched surface active sites [6] resulting from conjugation condensation in molten salts. Furthermore, the anisotropic ally distributed CN ring in the PHI structure can effectively promote charge delocalization, separation, and transmission, different from the low-crystallinity and

* Corresponding author.

** Corresponding author at: School of Environmental Science and Engineering, Sun Yat-sen University, Guangzhou 510275, China.

E-mail addresses: Zhaohn@mail2.sysu.edu.cn (H. Zhao), hechun@mail.sysu.edu.cn (C. He).

¹ ORCID: 0000-0002-3875-5631

incomplete-aggregation melon arranged in a zigzag pattern [7]. Guo et al. [8] synthesized PCNNs-IHO with well-ordered in-plane structures in NaCl molten salt. Due to the robust structural base sites provided by Na ions, PCNNs-IHO showed remarkable photocatalytic activity for CH₃SH mineralization under visible light. The heptazine ring structure of PHI facilitates the rapid migration of intrinsic carriers and shows promising application in photocatalytic removal of S-VOCs. However, in addition to enhancing the utilization of light, the adsorption and activation of S-VOCs on their inert CN surfaces still need to be improved (the catalytic reaction always takes place at the surface/interface of the catalyst). Recently, the coupling of transition metals (TMs) as co-catalysts with photocatalysts is an effective strategy to enhance the photocatalytic activity due to their unique "electron pump" effect. In this TMs-CN system, the external TMs NCs can act as "electron pump", effectively attracting photogenerated electrons from CN and facilitating charge redistribution at heterogeneous interfaces. Moreover, TMs act as active sites to change the surface reaction kinetics, thereby enhancing charge interactions between photocatalysts and adsorbed molecules [9, 10]. Moreover, the charge interactions between d-orbital electrons of transition metal and p-orbital electrons of adsorbed molecules can further facilitate the activation of molecules and regulated the ease of redox [11]. On the one hand, according to the Gibbs-Wolff principle, different exposed crystalline facets have different surface energies [12], making them have different pumping abilities for carriers excited inside the photocatalyst. On the other hand, different facets with different atomic arrangements and coordination have different electronic structures and surface reactive sites [13], which are essential for the activation of adsorbed molecules. Representatively, Wu et al. constructed Cu (111 +100) composite nanocrystals, which enhanced the selectivity and yield of C₂ products by enhancing the adsorption of *CO and lowering the activation energy barrier of C-C coupling [14]. Wang et al. prepared atomically dispersed transition metal-anchored nitrogen-doped carbon (M-N-C) catalysts and verified that Ni²⁺ in Ni-N-C SAC promoted electron transfer from C to Ni atoms in CO₂ and effectively activated the surface-adsorbed CO₂ [15]. Therefore, controlling the different exposure facets of TMs and compounding with PHI as model catalysts to utilize the electron pump effect of TMs is a potentially effective strategy for enhancing the photocatalytic minimalization of S-VOCs.

Herein, a series of model photocatalysts were synthesized by coupling different facets exposed of Cu nanocrystals (Cu (111), Cu (100), Cu (111 +100)) with PHI and used for photocatalytic elimination of CH₃SH. We observed that the Cu (111)/PHI exhibited a much higher photocatalytic activity than that of PHI, Cu (100)/PHI, and Cu (111 +100)/PHI, respectively, and was superior than the other reported CH₃SH elimination technologies. Time-resolved photoluminescence decay (TR-PL) and Femtosecond time-resolved transient absorption spectroscopy (fs-TAS) analysis were carried out to understand the intrinsic carrier excitation and the ultra-fast electron transfer kinetics. DFT calculations were used to explain the ability of generation ROS during photocatalytic processes and find out CH₃SH, H₂O, and O₂ differed in adsorption and activation on Cu (111)/PHI surfaces. In situ XPS is further used to probe the specific impact of Cu (111)-enhanced electron pump effects on photogenerated charge transfer as well as the stronger electron interaction with the adsorbed molecules. Overall, this study highlights the synergistic engineering strategy between facet engineering and ultrafast internal dynamics, which facilitates carrier utilization during photocatalytic elimination of S-VOCs and provides a new opportunity for improving charge carrier dynamics and photocatalytic performance.

2. Experimental details

2.1. Preparation of catalysts

The fabrication process of Cu (111)/PHI through the two-step method was illustrated in Fig. 1a. Briefly, 50 mg of PHI was added to

50 mL deionized water, followed by ultrasonication for 10 min to obtain a homogeneous solution. Subsequently, 12 mg of Cu (111) NCs along with 30 mg of ascorbic acid were added into the suspension and mixed homogeneously by ultrasonication. The mixture was transferred to an oil bath pot, which maintained at 90 °C for 12 h and naturally dropped to room temperature. Finally, the obtained products were washed several times with deionized water and dried at 60 °C for 12 h in the vacuum oven. The obtained solid products were denoted as Cu (111)/PHI. For comparison, the preparation of Cu (100)/PHI and Cu (111 +100)/PHI followed a similar procedure as Cu (111)/PHI, except that Cu (111) NCs was replaced with Cu (100) NCs and Cu (111 +100) NCs, respectively. A detailed account of the preparation process for other catalysts was provided in Supporting Information (SI).

2.2. Photocatalytic elimination of CH₃SH

Photocatalytic elimination of CH₃SH was carried out in a fixed-bed quartz photoreactor under atmospheric pressure (Scheme S4). 50 mg catalyst was fixed between two quartz wool plugs of photoreactor. The reactant (40 ppm CH₃SH mixed with Air, total flow rate = 10 mL/min) was fed to the reactor and the gas mixture was passed through the catalyst for 30 min to reach the adsorption equilibrium before light irradiation. A 300 W xenon lamp (PLS-SXE 300/300UV, Perfect Light, China) with full-wavelength was used to simulated AM 1.5 G illumination (100 mW/cm⁻²) into the quartz reactor from the top (12 cm from the quartz reactor window). And the CH₃SH concentration at the outlet of the device was recorded every minute and the CH₃SH elimination rate (η) was calculated by the following equation [16]:

$$\eta (\%) = \left(1 - \frac{C}{C_0}\right) \times 100\% \quad (1)$$

Where C, C₀ represent the concentration of CH₃SH at the outlet and the initial concentration, respectively.

3. Results and discussion

3.1. Characterization of catalysts

X-ray diffraction (XRD) was utilized to investigate the crystal structure of catalysts. The results in Fig. 1b indicated that Cu NCs exhibited good crystallinity, with diffraction peaks at 43.2°, 50.4°, and 72.2° corresponding to Bragg reflections of (111), (200), and (220) facets of metallic Cu (JCPDF # 04-0836) [17], respectively. Rietveld refinement (Fig. S1a) confirmed that Cu (111) NCs had a single crystal structure. With regard to Cu (111 +100) NCs, the diffraction peak at approximately 27.1° was attributed to the (111) facet of Cu₃O₄ [18], manifesting that the species was mixed-crystalline. The slight shift between (111) and (200) facet was mainly due to the difference in the surface formation energy of mixed crystals. However, Cu (100) NCs exhibited low crystallinity, indicating that it is poorly stabilized structurally and easily oxidized by O₂ and H₂O in air. And the (111): (200) peak intensity ratio of the Cu (111) NCs was significantly higher than that of the Cu (100) NCs, indicating that (111) was the mainly exposed facet of the sample. Similarly, a relatively high (100): (111) ratio indicated that (100) was the dominant facet in Cu (100) NCs, and Cu (111 +100) NCs exhibited similar (111) and (100) peak intensities. Additionally, the diffraction peaks located at 41° and 66° corresponding to KCl and LiCl (Fig. S1b). After the composite formed (Fig. 1c), the diffraction peaks of KCl, LiCl, and Cu NCs weakened or even vanished, verifying the successful preparation of Cu/PHI with different exposed facets. Fig. 1d depicted the structural model of pure PHI and Cu (111)/PHI, which will be used for the subsequent DFT calculations.

Fourier transform infrared spectroscopy (FTIR) was employed to examine the surface chemical composition of the prepared photocatalysts. As depicted in Fig. 1e, the heptazine ring derivatives

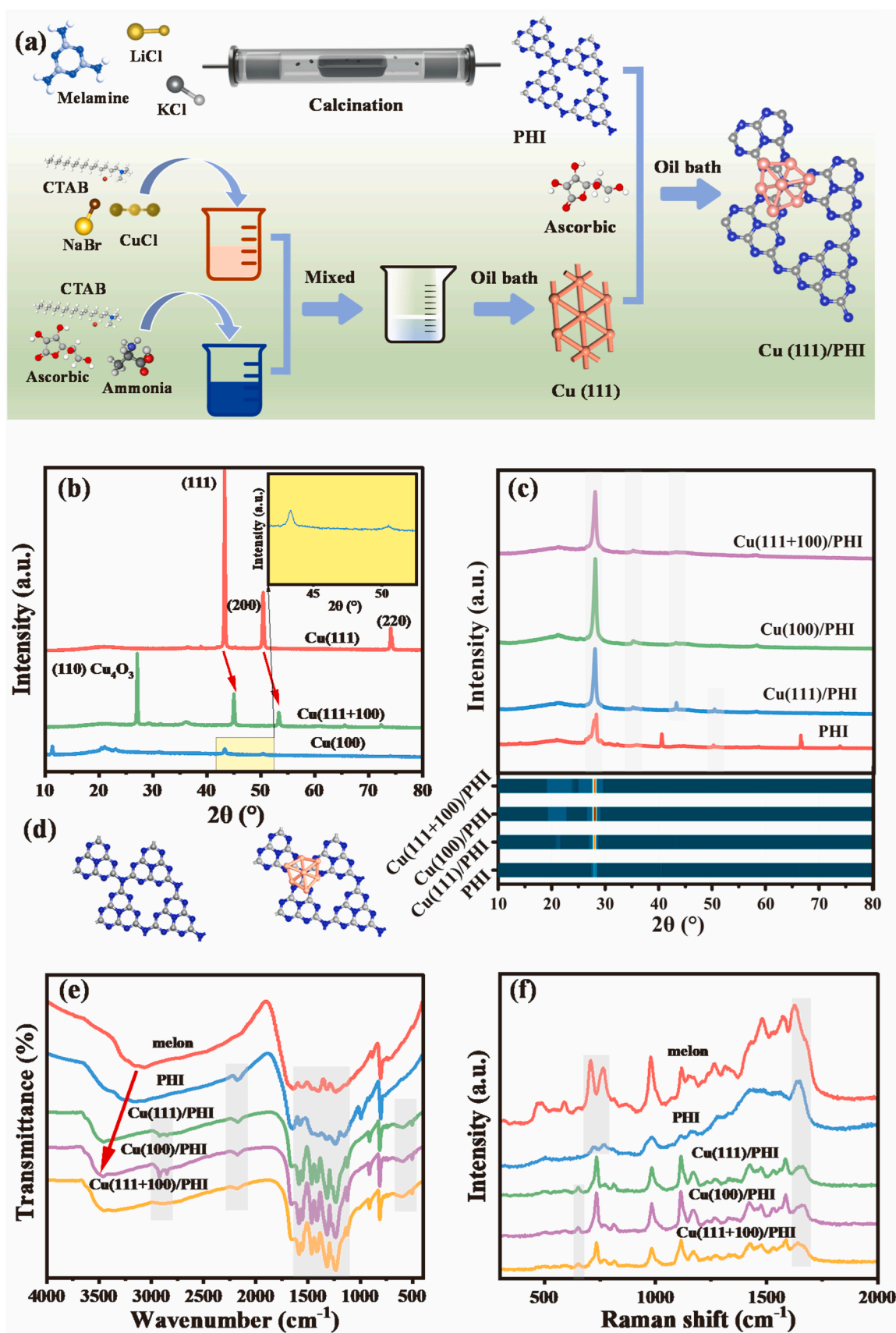


Fig. 1. (a) The schematic diagram for the synthesis of Cu (111)/PHI; Partial XRD patterns of (b) Cu NCs with different facet, (c) PHI, Cu (111)/PHI, Cu (100)/PHI and Cu (111 +100)/PHI; (d) Molecular structure of PHI and Cu (111)/PHI; (e) FTIR spectra and (f) UV Raman spectra of the as-prepared catalysts.

stretching mode produced fingerprint peaks within the 1200 – 1700 cm^{-1} range, and the enhanced vibrational intensity of Cu NCs composition compared to PHI was ascribed to its planarization of the in-plane conjugated system. Additionally, surface adsorbed water caused a broad absorption band between 3000 – 3500 cm^{-1} . The vibrational peaks at 502, 615 and 2900 cm^{-1} within the composite catalyst were attributed to the tensile vibration of Cu(I)-O, asymmetric vibration of Cu-N bond, and the vibrational peak caused by unsaturated coordination of Cu-N [19], respectively, demonstrating that Cu forms a tight heterostructure by binding to N on the surface of PHI [20]. In contrast, the vibrational peak at 2175 cm^{-1} was only observed in the PHI sample bound to molten salt, suggesting the presence of a small number of unreacted or terminal -CN groups on the catalyst surface during preparation by the K and Li molten salt method [21]. UV Raman spectra confirmed the basic structural pattern of catalysts, with various characteristic peaks of melon noted at 710, 769, 980, 1117, 1270, 1481, 1576, and 1629 cm^{-1} , representing the vibration of aromatic C-N heterocycle and ring breathing modes of s-triazine [22] (Fig. 1f). For PHI, the C-N skeleton was notably changed, indicating that the successful formation of heptazine ring. Cu NCs coupling with PHI resulted in a newly appeared peak located at the 655 cm^{-1} position, corresponding to the Cu(1)-O bond [23]. Furthermore, the plasmon resonance effect after Cu NCs loading caused a red shift of the peak located at 1629 cm^{-1} to 1664 cm^{-1} .

Scanning electron microscope (SEM) and transmission electron microscopy (TEM) showed the Cu (111), Cu (100) and Cu (111 +100) NCs exhibited triangular sheet (Fig. 2a and Fig. S2a), nano-cube (Fig. S2b) and tetragonal nanosheet (Fig. S2c), respectively, with an average edge length of $\sim 2.0 \pm 0.5 \mu\text{m}$ [24]. The lattice spacing in filtered images of 0.209 nm on its surface correspond to Cu (111) facet, while 0.248 nm corresponds to the Cu_2O (111) facet (Fig. 2b) [25]. The composition catalyst showing increased surface roughness (Figs. S2d-2f and Fig. 2c-d) [26], and the same lattice spacing indicates that the coupling of Cu (111) NCs with PHI did not change their crystal structures. Energy dispersive spectrometer (EDS) analysis of Cu (111) NCs, Cu (111 +100) NCs (Fig. S3) and Cu (111)/PHI confirmed that elements were uniformly dispersed (Figs. 2e and 2f) [27], further implying that Cu (111) NCs and PHI form a tight composite structure. In addition, Cu (111)/PHI has a larger specific surface area and smaller mesoporous structure (Fig. S4, Table S1), which is favorable for enhancing the mass transfer of small molecules.

Surface electronic states of catalysts were examined by X-ray photoelectron spectroscopy (XPS). All signals of C, N, O, and Cu elements can be seen in the XPS survey scan of the catalysts (Fig. S5a). For the high-resolution C 1s spectra, three characteristic peaks at 284.7,

286.1 and 288.3 eV were attributed to sp^2 C-C bonds, C-O bond and sp^2 -bonded carbon from N-containing heptazine ring (N-C = N) [28], respectively. The peaks in the PHI at 295.6 and 292.8 eV corresponded to the K 2p orbital, which disappeared after Cu loading (Fig. 3a), suggesting that the K ions were masked by Cu NCs and become difficult to recognize. The N 1s spectrum could divide into two distinct peaks at 400.7 and 398.7 eV, which corresponded to C=N-C and H-N-C [29], respectively (Fig. 3b). This indicated that the basic structure of PHI not changed after coupling with Cu NCs, implying that there was no change in the structure of PHI due to surface chemical bonding between Cu and PHI. The Cu 2p peaks recorded in the catalyst primarily presided in Cu^0 (932.8 and 952.7 eV), while a small amount of Cu^+ oxidation states (934.6 and 954.5 eV) arose due to surface oxidation [30], and there were two satellite peaks located at 943.1 eV and 944.9 eV (Fig. 3c). Auger electron spectroscopy (AES) indicated that the signal predominantly arose from Cu_2O [24]. The fitting of the Cu LMM profiles revealed that the Cu^0/Cu^+ ratios in Cu (111 +100)/PHI, Cu (100)/PHI and Cu (111)/PHI were 2.31, 4.15, and 1.82, respectively (Fig. 3d). The smaller ratio of Cu^0/Cu^+ enhanced the electron extraction, which led to faster electron transfer to the active sites on the catalyst surface and participated in the redox reaction, thus promoting the self-cycling of Cu^0/Cu^+ and enhancing the cycling performance of the catalyst [31]. And the Cu^+ presence was mainly due to the O-H bond of surface-adsorbed water and C-O bond from adsorbed O species interacting with the C atom [28] (Fig. S5b).

3.2. Photocatalytic performance of CH_3SH elimination

Fig. 4 and Fig. S6 displayed the CH_3SH elimination rates of different photocatalysts under PCO process. Before the photocatalytic degradation experiments, the catalyst samples were first adsorbed on CH_3SH for 30 min to reach the adsorption equilibrium state (Fig. S6a). The elimination efficiency of CH_3SH was poor (2.3% per 30 min) by SSL. In contrast, PHI achieved 60.4% removal of CH_3SH within 30 min, much higher than that of melon (27.8%) (Fig. S6b, Figs. 4a and 4b), which indicated that the heptazine ring structure had a more superior activity in the degradation of CH_3SH . After coupled with PHI, the elimination efficiency of Cu (111)/PHI increased to 87.8% per 30 min, while Cu (100)/PHI and Cu (111 +100)/PHI showed elimination rates of CH_3SH at 71.5% per 30 min and 70.4% per 30 min. This elimination efficiency was superior to other techniques that have been reported for the elimination of CH_3SH (Table S6). In order to simulate the actual operating environment and explore the practical application prospects of the catalysts, the photocatalytic activities were investigated under different catalyst dosages and different ambient humidity conditions, respectively. As depicted in Figs. 4c and 4d, the elimination efficiency of CH_3SH gradually increased with a significant increase in catalyst dosage, and there was a linear relationship between the dosage and elimination efficiency. Furthermore, we investigated different amounts of Cu (111) NCs coupled with PHI to further investigate the role of Cu NCs. In Fig. S7a, the adsorption capacity of Cu (111)/PHI system for CH_3SH gradually increased with the increase of Cu (111) NCs loading (from 10% to 30%, wt%), which is attributed to the fact that more Cu NCs load provides more active metal sites. In the process of photocatalytic CH_3SH elimination (Fig. S7b), 20% Cu (111)/PHI exhibited the best photocatalytic activity, higher than that of 10% Cu (111)/PHI (73.1%) and 30% Cu (111)/PHI (79.4%). This may be due to more surface Cu being oxidized to form a "passivation layer", which hinders the effective utilization of photogenerated carriers.

In addition, the activity of Cu (111)/PHI was slightly increased at RH = 15% (88.9% per 30 min), which could be attributed to the small amount of H_2O involved in the radical reaction generating more ROS before competing with CH_3SH in high RH condition. In contrast, the activity of Cu (100)/PHI and Cu (111 +100)/PHI decreased at RH = 15%, which could be attributed to the fact that Cu (100) and Cu (111 +100) have a higher surface energy than that of Cu (111) and

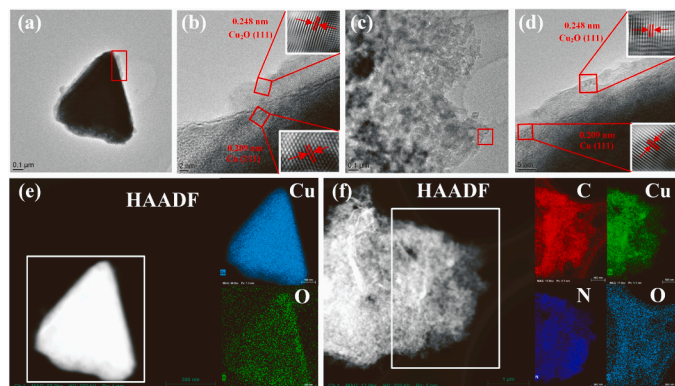


Fig. 2. (a) TEM image of Cu (111) NCs; (b) HR-TEM images of Cu (111) NCs (Inset: Filtered images of lattice spacing); (c) TEM image of Cu (111)/PHI; (d) HR-TEM image of Cu (111)/PHI (Inset: Filtered images of lattice spacing); HAADF-STEM image of (e) Cu (111) NCs, (f) Cu (111)/PHI and corresponding elemental mappings of C, Cu, N, O.

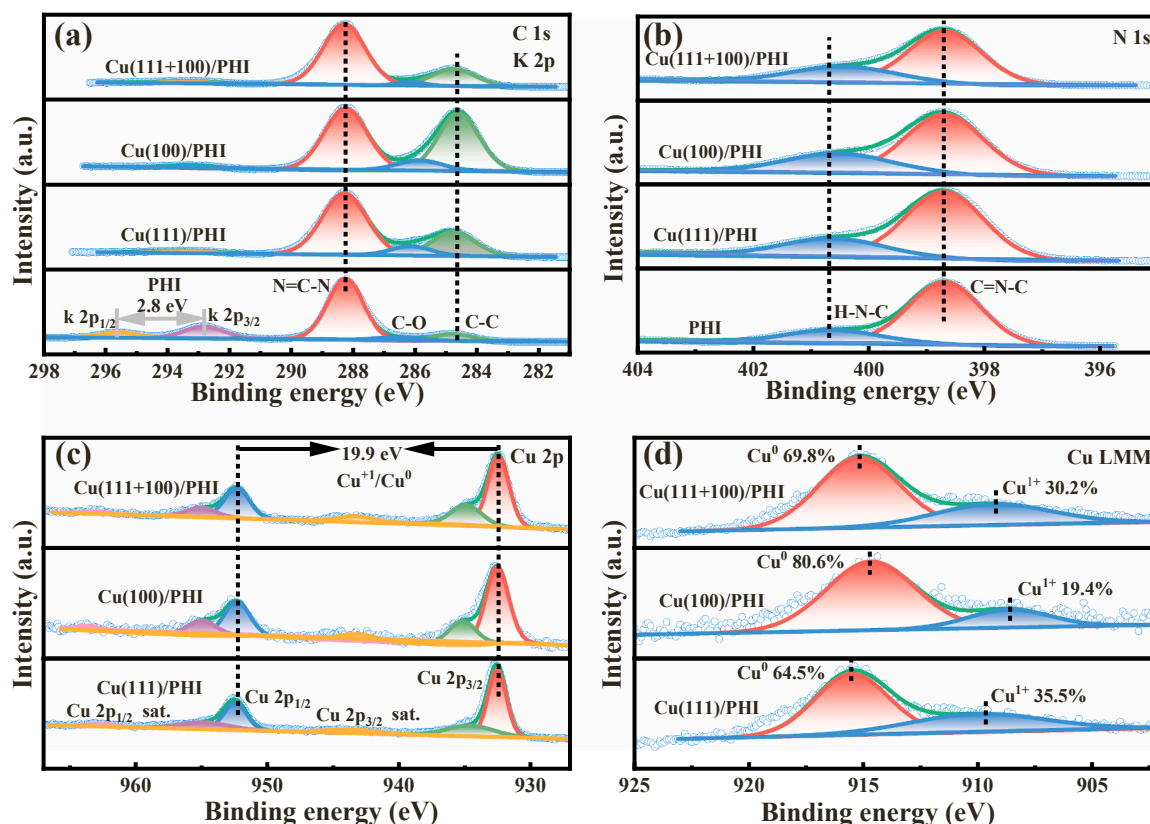


Fig. 3. High-resolution XPS spectra of (a) C 1s, (b) N 1s, (c) Cu 2p, (d) Cu LMM of the as-prepared photocatalysts.

lower abundance of Cu atoms on the surface, which makes them less tolerant to H_2O molecules. And the catalytic activity decreased dramatically with increasing humidity, indicating that competitive adsorption of H_2O hinders the elimination of CH_3SH by the catalyst. The stability and durability of the catalysts are also important indicators to evaluate their merits [1]. The stability test presented that the catalytic performance dropped only slightly from 87.8% to 83.3% (Fig. S8a) after 450 min (The reason for choosing 450 min is to balance the time cost and photocatalytic stability assessment during the experimental process.) of continuous operation, and the results indicated that Cu (111)/PHI has good durability. Furthermore, SEM (Fig. S8b), XPS (Fig. S9a), and XRD (Fig. S9b) tests of the Cu (111)/PHI after reaction showed that the physical structure and crystal structure did not change significantly. The high-resolution XPS spectra showed that the C and N elements remained stable (Fig. S10a and S10b) and only acted as photogenerated electron sources, while Cu showed a trend of Cu^0/Cu^+ becoming larger (Fig. S10c and S10d), which may be ascribed to the higher VB potential in Cu (111)/PHI ($\text{VB} = +2.06 \text{ V}$) than the redox potential of Cu^0/Cu^+ (0.52 V) [32]. As a result, Cu (111) NCs prepared by rational design in this study do not undergo significant oxidation even after a long-term period of operation, and thus maintain the high activity and stability of Cu (111)/PHI composite photocatalyst.

3.3. Reactive oxygen species (ROS) and charge transfer kinetics

In general, the photocatalytic performance is closely correlated to the formation and conversion of ROSs like singlet oxygen ($^1\text{O}_2$), hydroxyl radical ($\bullet\text{OH}$), and superoxide anion ($\bullet\text{O}_2^-$), prompting CH_3SH photocatalytic elimination and final mineralization. Herein, electron paramagnetic resonance (EPR) analysis was conducted to detect ROS generated of $^1\text{O}_2$, $\bullet\text{O}_2^-$, and $\bullet\text{OH}$ in various systems, respectively. In Fig. 5a, a weak TEMO- $^1\text{O}_2$ intensity signal was detected under dark conditions. After 5 min of irradiation (Fig. 5b), the intensity signals of

TEMPO- $^1\text{O}_2$ 1:1:1 triplet peak were detected to be enhanced in all system [33], and Cu (111)/PHI showed the highest peak, indicating that a large amount of $^1\text{O}_2$ was generated. As shown in Fig. 5c, DMPO- $\bullet\text{OH}$ signals were not detected in the dark meant that electron transfer is weaker under dark conditions. However, after 5 min of irradiation, a strongly 1:2:2:1 quadruple peak was detected in Cu (111)/PHI system (Fig. 5d), attributing to the DMPO- $\bullet\text{OH}$ complex [34]. And the stronger characteristic signal observed in Cu (111)/PHI system showed that the amount of $\bullet\text{O}_2^-$ was much more than other systems in dark conditions (Fig. 5e) and light irradiation (Fig. 5f), indicating that the enhanced electron pump effect of Cu (111) facet can effectively activate small molecules and generate abundant free radicals. According to the EPR analysis, the CH_3SH elimination by Cu (111)/PHI mainly relied on the $^1\text{O}_2$, $\bullet\text{OH}$ and $\bullet\text{O}_2^-$, the different concentration of ROS may be attributed to that Cu (111) nanocrystal has the strongest electron pump effect and more surface defects of Cu (111)/PHI [35] (Fig. S11), which makes a quite difference in the adsorption and activation capacity of the two for small molecules such as H_2O and O_2 .

The discrepancy in photocatalytic activity of several catalysts and the reasons behind the variations in generation of ROS were investigated by the optical and photoelectrochemical properties [36]. The flat-band potentials of the prepared photocatalysts were tested by Mott-Schottky (Fig. S12a and S12b, Fig. S13a), and it was found that PHI had a higher flat-band potential ($E_{\text{fb}} = -1.03 \text{ eV}$) than melon ($E_{\text{fb}} = -0.75 \text{ eV}$), while Cu (111)/PHI has the lowest flat-band potential ($E_{\text{fb}} = -0.56 \text{ eV}$) than Cu (100)/PHI ($E_{\text{fb}} = -0.63 \text{ eV}$) and Cu (111 + 100)/PHI ($E_{\text{fb}} = -0.70 \text{ eV}$). The positive slopes of the Mott-Schottky curves for both catalysts indicated that they are n-type semiconductors, and the conduction band (CB) potential of n-type semiconductor is 0.2 eV more negative than the flat-band potential [37]. As determined from the transformed Kubelka-Munk function [38], the band gap of the composite catalyst is narrower than that of melon ($E_{\text{g}} = 2.67 \text{ eV}$) and PHI ($E_{\text{g}} = 2.68 \text{ eV}$) (Fig. S13b and S13c). Furthermore, the valence band (VB)

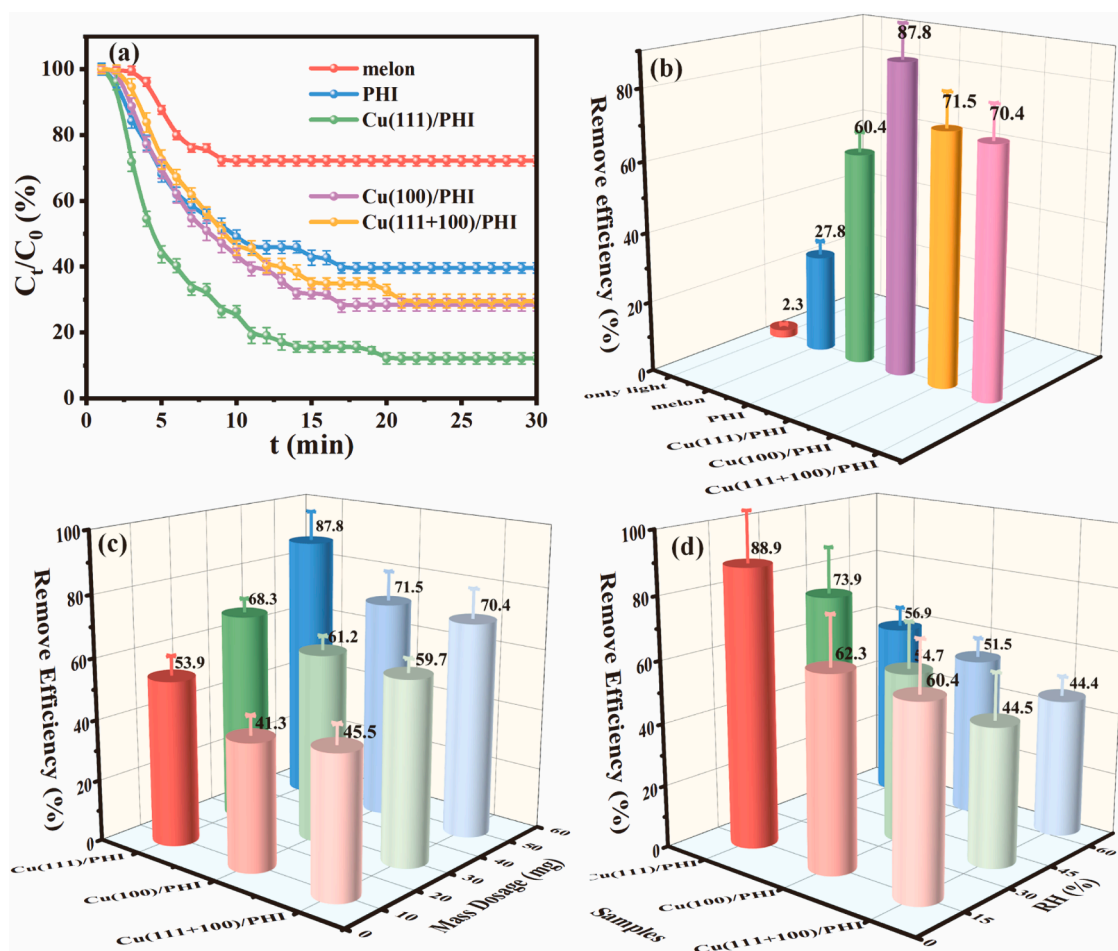


Fig. 4. (a) Photocatalytic elimination of CH_3SH with different catalysts; (b) Elimination efficiency with different catalysts; (c) Effect of catalyst dosage and (d) Relative humidity (RH) on photocatalytic elimination of CH_3SH with different photocatalysts.

potentials of all catalysts were calculated according to the equation [39]:

$$E_{CB} = E_{VB} - E_g \quad (2)$$

The change in band gap structure resulted in the modulation of the redox ability of catalysts, and Cu (111)/PHI had the most positive VB potential ($E_{VB} = +2.06$ eV), higher than that of Cu (100)/PHI ($E_{VB} = +2.03$ eV) and Cu (111 +100)/PHI ($E_{VB} = +1.87$ eV), indicating the strongest oxidation ability of Cu (111)/PHI. The optimized band gap structure of catalyst led to the optimization of its intrinsic conductivity and photogenerated carrier density, as evidenced by the reduction of the interfacial electrochemical impedance and the enhancement of the transient photocurrent. In EIS spectra (Fig. 6a), Cu (111)/PHI displayed the smallest single semicircle radius with interfacial charge transfer impedance. The EIS data were further fitted using an equivalent circuit to estimate the R_p , indicating that there was a single equivalent charge transfer process during the reaction [40]. And the values of 311.5 Ω , 434.3 Ω , and 468.4 Ω for Cu (111)/PHI, Cu (100)/PHI, and Cu (111 +100)/PHI, respectively (Table S2). Upon light illumination, the arc of the semicircle turned smaller than that at dark (Fig. S14a), which proved that illumination functions as the intrinsic driving force for carrier excitation and further improved the charge separation and transfer processes. Meanwhile, Linear sweep voltammetry (LSV) tests revealed that Cu (111)/PHI had the largest current density (Fig. S14b), meaning large electrons in the system. Similarly, Cu (111)/PHI exhibited the strongest transient photocurrent response, implying that it had the highest carrier concentration (Fig. 6b).

Steady-state photoluminescence (PL) and time-resolved

photoluminescence decay (TR-PL) spectra were used to investigate the interfacial charge transmission dynamics. As exhibited in Figs. 6c and 6d, PHI showed a higher PL intensity indicated the rapid recombination of photogenerated carriers. Conversely, the PL intensity of the composite catalyst decreased gradually due to the electron pump effect of the Cu nanocrystals [41], thereby enhancing the separation of photogenerated electron-hole pairs. The fits of the emission decay curves from Cu (111)/PHI catalysts indicated that their exciton lifetimes were significantly shorter than those of the PHI catalysts. Specifically, the lifetime parameter decreased substantially from $\tau_A = 3.325$ ns (PHI) to $\tau_A = 0.268$ ns (Cu (111)/PHI). The short lifetime in Cu (111)/PHI suggested the possibility of promoting photocatalytic CH_3SH oxidation due to the electron pump effect of Cu (111) nanocrystals. In conclusion, the sustained fluorescence quenching of the composited catalysts provides conclusive evidence for the critical role of Cu (111)-enhanced electron pump effect in facilitating interfacial charge transfer [42].

Femtosecond time-resolved transient absorption spectroscopy (fs-TAS) was used to deeply investigate the generation and transfer mechanisms of photogenerated electrons in PHI and Cu (111)/PHI fractions, thereby clarifying the intrinsic reason for the enhanced electron pump effect of Cu (111). Figs. 7a and 7d illustrated the pseudo-color TAS results obtained with a pump wavelength of 380 nm, while the corresponding TAS spectra (420–750 nm) captured at various representative probe delays (ranging from 1 ps to 5 ns) were presented in Figs. 7b and 7e [43]. A prominent negative stimulated emission (SE) distinctly appeared at 500 nm and a positive excited-state absorption (ESA) peak appeared at 620 nm after photoexcitation [44]. The SE signal was attributed to the 1S exciton band, corresponding to the photoinduced

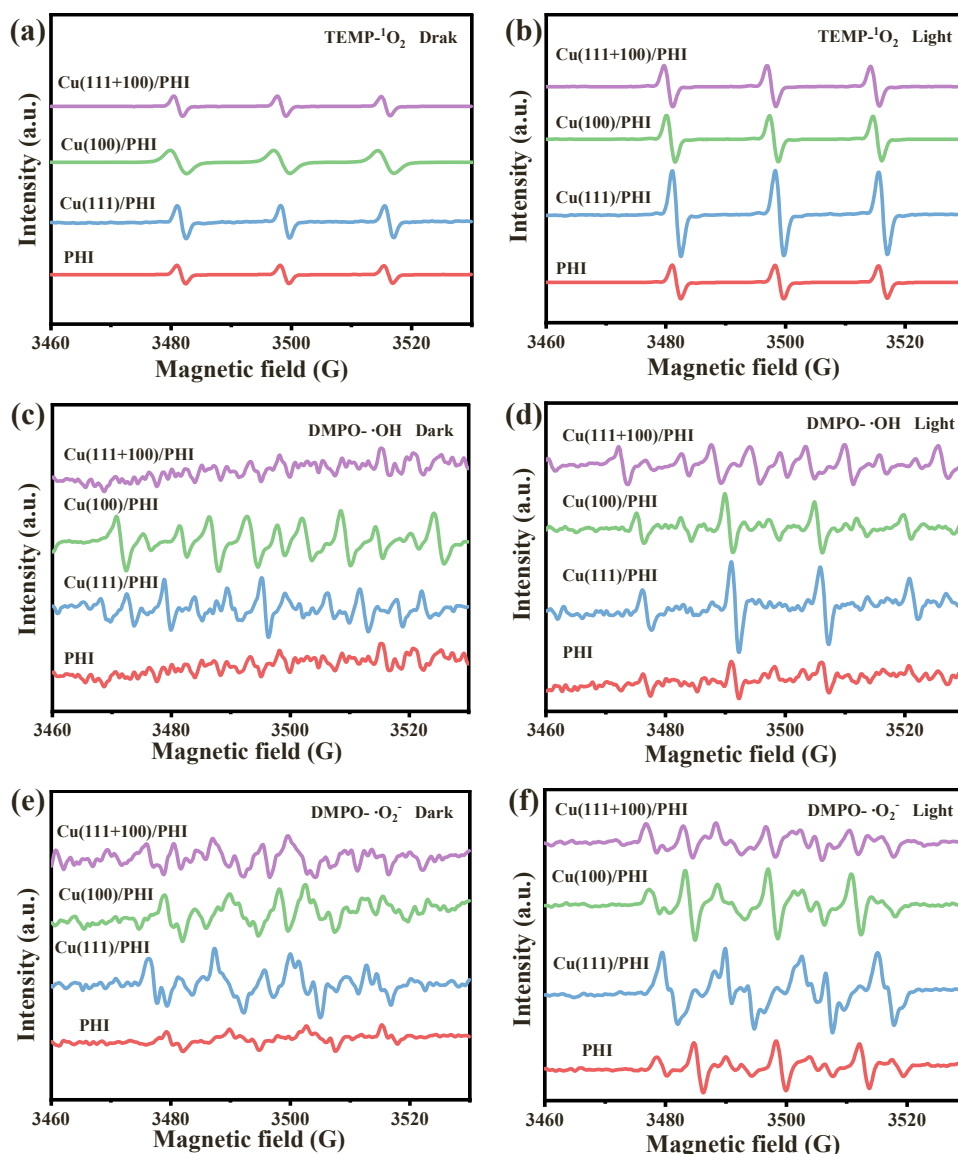


Fig. 5. EPR spectra of (a), (b) $^1\text{O}_2$; (c), (d) $\bullet\text{OH}$; (e), (f) $\bullet\text{O}_2$ under dark and light conditions in different systems.

charge transition from VB to CB [45]. Therefore, the stronger the negative characteristic absorption peak, the more charge carriers were generated. Similar to SE, the ESA features in visible wavelength region were mainly caused by the migration of photogenerated electrons or electron-hole pairs in the catalyst [46]. The SE and ESA characteristic absorptions were stronger in Cu (111)/PHI with different delay times, indicating that Cu (111) nanocrystal in Cu (111)/PHI system could effectively pump out electrons and suppress carrier complexation phenomena on ps scale. And time absorption curves normalized at 620 nm to compare the ultrafast kinetics of singlet excitons in PHI and Cu (111)/PHI (Fig. 7c and Table S3). Generally, for the co-catalyst/photocatalyst system, the whole process can be divided into two main regions, including short lifetime (τ_1) and long lifetime (τ_2), which corresponds to the process of electron capture by trap states (TS) (e.g., structural defects), and interfacial photoelectron transfer from the CB to the co-catalyst [47]. As expected, the exciton lifetime was shorter in PHI at 737.6 ps (τ_2) compared to 1394.5 ps (τ_2) in Cu (111)/PHI, indicating Cu (111) successfully prolonged the carrier relaxation time as an external electron pump during ESA process, and further promoted the photocatalytic reaction kinetics of elimination CH_3SH . When quizzed the temporal absorption profile at 500 nm, the extended lifetime of the

charge-separated state (Fig. 7f) was observed. The lifetime of Cu (111)/PHI was 663.9 ps (τ_2), longer than that of PHI (316.0 ps, τ_1), which was mainly attributed to the rapid jump of photogenerated electrons from VB to CB [48]. In this case, the formation of built-in electric field accelerated the photogenerated electrons jumped to CB jump and prompted electrons migrated to the surface-active site due to the enhanced electron pump effect of Cu (111) nanocrystal.

The charge transfer in PHI and Cu (111)/PHI were further detected by in situ synchrotron illumination XPS, which in turn elucidated the mechanism of electron pump-enhanced charge transfer under optimal conditions. Fig. 8a-c displayed that no change in the binding energy of C, N, and O elements before and after illumination over PHI, indicating a strong internal carrier complex that has difficulty in overcoming the Coulomb resistance to reach the catalyst surface [49]. During the in-situ light-induced XPS tests of single-component semiconductors, the carbon conductive band can act as an electron trap, showing that light-generated electrons flow from the photocatalyst to the carbon conductive band and eventually to the sample loader. Therefore, an equilibrium has been reached with the electron influx into PHI and the electron flow from it to the substrate, resulting in no significant external electron density change [50]. Under continuous illumination, Cu

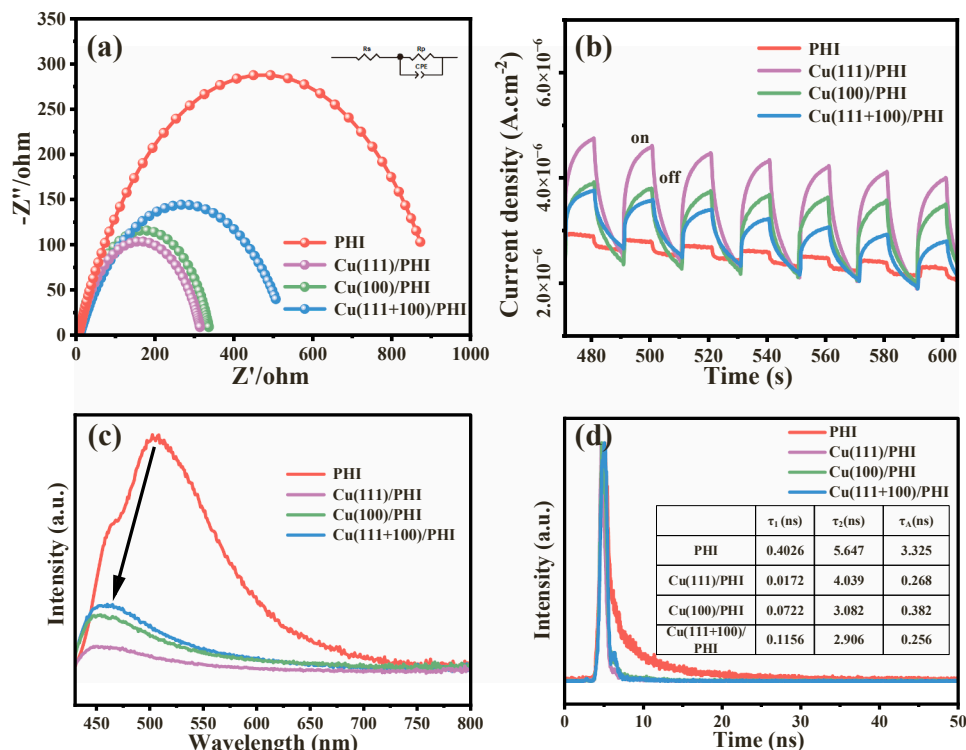


Fig. 6. (a) Electrochemical impedance spectroscopy (EIS) spectra; (b) Transient photocurrent density; (c) Steady-state photoluminescence (PL) and (d) Time-resolved photoluminescence decay (TR-PL) spectra of the as-prepared photocatalysts.

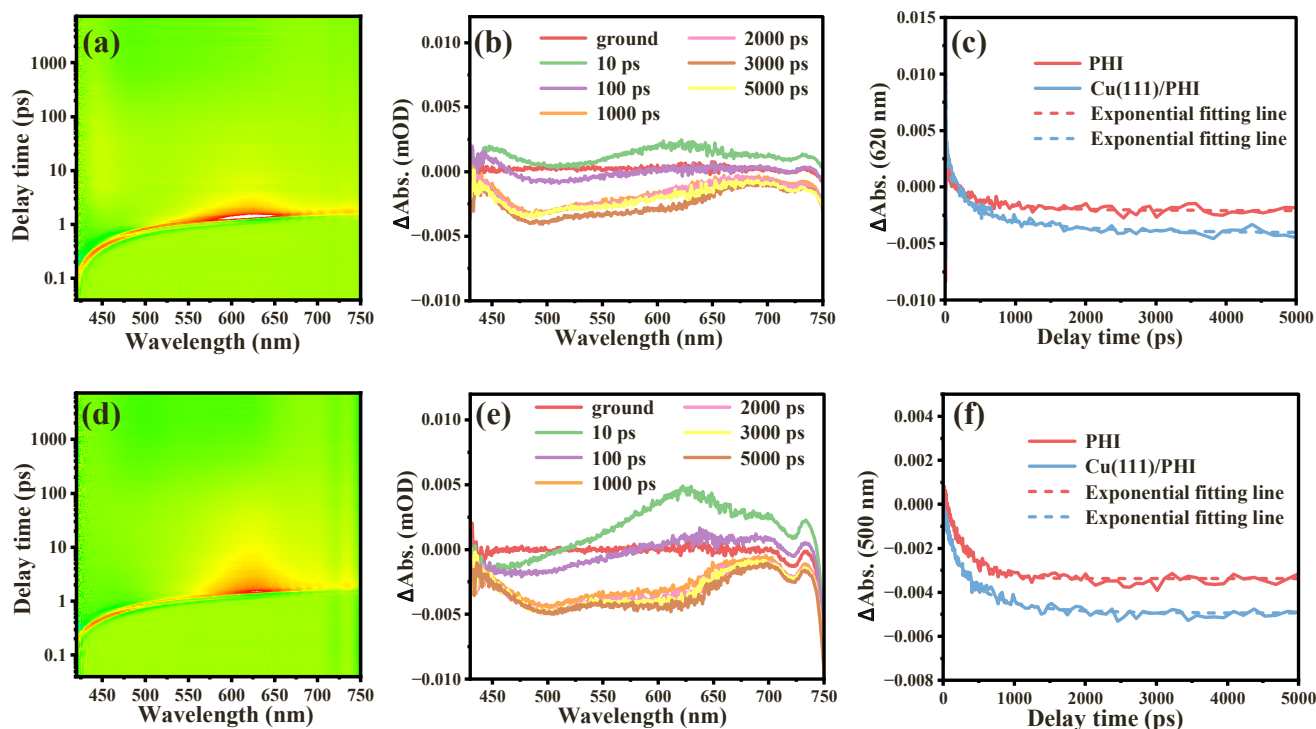


Fig. 7. The pseudo-color plots of fs-TAS observation: (a) PHI and (d) Cu (111)/PHI in ethanol (pump laser: 380 nm); TAS spectra signals of (b) PHI and (e) Cu (111)/PHI on the ps timescales; The typical TA kinetics probed at (c) 620 nm and (f) 500 nm for PHI and Cu (111)/PHI.

(111)/PHI performed a positive shift of 0.1 eV in the binding energies of C and N (Figs. 8d and 8e), while O and Cu showed a negative shift of 0.2 eV and 0.1 eV, respectively (Figs. 8f and 8g), implying that the carbon atoms suspended around the nitrogen continuously donate

electrons through Cu (111) and provided electrons to the antibonding orbitals of the adsorbed oxygen species, and the O1s spectrum shifted significantly to a lower binding energy of 0.2 eV, where the surface Cu-N bond acts as an electron bridge, and the surface oxygen participates in

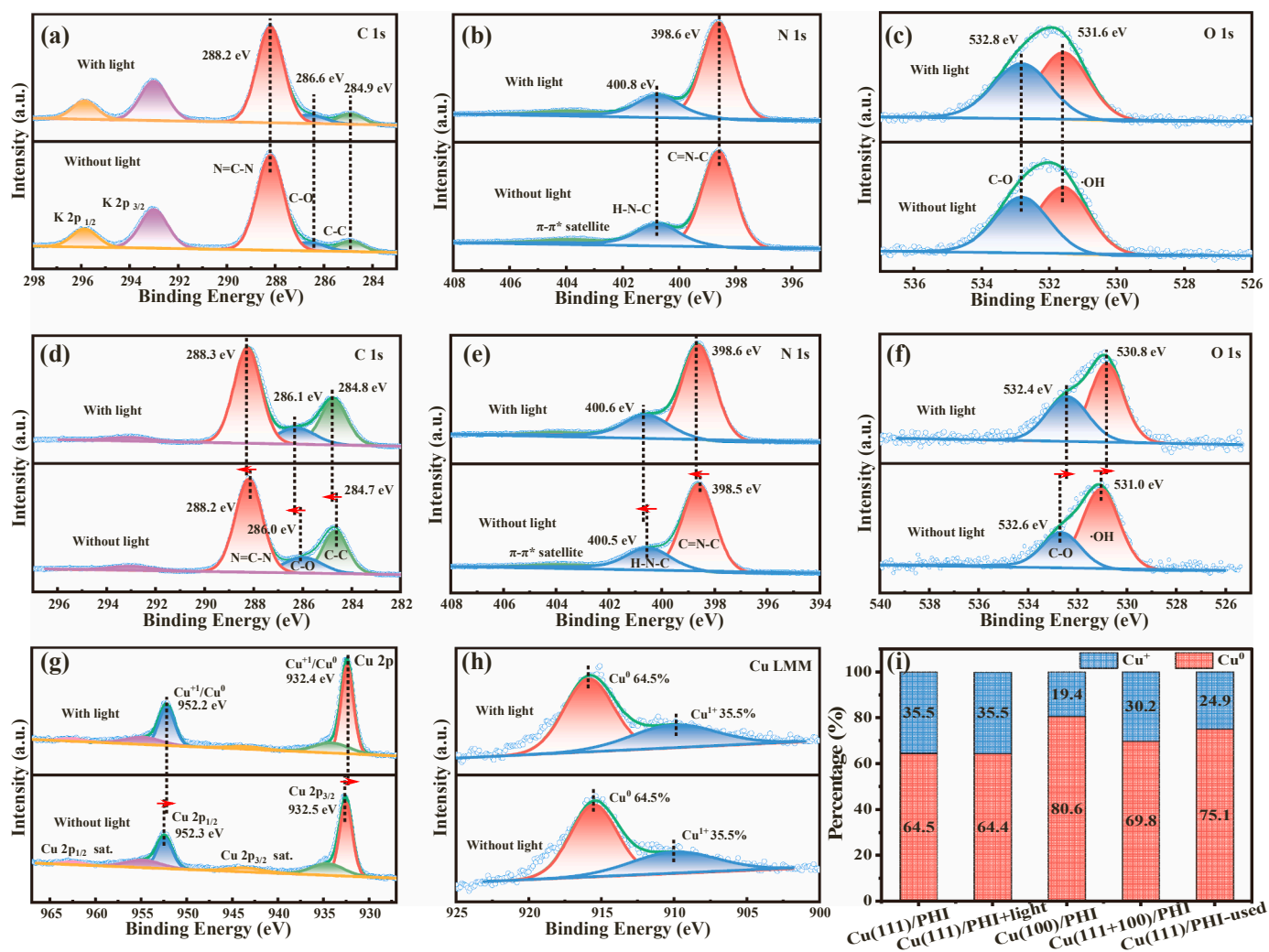


Fig. 8. In-situ XPS spectra of (a) C 1 s, (b) N 1 s and (c) O 1 s without light irradiation (bottom) and with irradiation (top) for PHI; In-situ XPS spectra of (d) C 1 s, (e) N 1 s, (f) O 1 s, (g) Cu 2p and (h) Cu LMM without light irradiation (bottom) and with irradiation (top) for Cu (111)/PHI; (i) Cu content in the as-prepared catalysts.

the reaction [51]. Further analysis of the Auger spectra of Cu showed that the Cu⁰/Cu⁺ ratio did not change before and after illumination, a result showed that Cu only played a role in the photocatalytic process of electron abstraction and transfer (Figs. 8h and 8i). Due to its minimal Cu⁰/Cu⁺ ratio, electrons can quickly transfer through the interface Cu-N bridge to the active sites, and participate in subsequent redox reactions. In contrast, Cu (100)/PHI and Cu (111 +100)/PHI have higher Cu⁰/Cu⁺ ratios, causing the photogenerated electrons to first participate in the internal Cu sites before transferring to the surface-active sites, resulting in lower carrier mobility and utilization, and decreased photocatalytic activity. The coupling of Cu (111) nanocrystals with PHI only acted as an external electron pump, which accelerated the existence of a space charge region at the PHI and Cu (111) interface and promoted the rapid and efficient transfer of light-induced electrons to the surface-active sites at the ps level.

3.4. Photodegradation product research

In-situ diffuse reflectance Fourier transform infrared spectroscopy (In-situ DRIFTS) experiments were performed to investigate the CH₃SH adsorption and oxidation on various catalysts. During the adsorption process (Figs. 9a and 9c), a series of peaks associated with the adsorption and conversion of CH₃SH emerged, confirming the interaction between PHI or Cu (111)/PHI and CH₃SH, resulting in the oxidation of a minimal proportion of CH₃SH [52]. Specifically, the peaks located at

752 and 822 cm⁻¹ correspond to the vibration of the C-S bond in CH₃SH, the peaks at 954 and 1003 cm⁻¹ correspond to the asymmetric stretching vibration of SO₃²⁻ and CH₃S-SCH₃, the peaks at 1319 and 1320 cm⁻¹ correspond to the vibration of the O=S=O group in the sulfonate species, the peaks at 3440 cm⁻¹, 3460 cm⁻¹ correspond to the presence of adsorbed water on the catalyst surface. The strong peaks at 1200–1500 cm⁻¹ correspond to the characteristic stretching of C-N in the heptazine ring [53]. The other peaks located at 1455, 1529, and 1687 cm⁻¹ are attributed to the bending peak of -CH₃, the bidentate carbonate peak, and the vibrational peak of SO₄²⁻ [54], indicating the accumulation of CH₃SH molecules as well as some intermediate products on the surface during the adsorption process. In contrast, during the adsorption process of Cu (111)/PHI, there was a distinct new peak observed at 2334 cm⁻¹ corresponded to the adsorbed CO₂, indicating the higher oxidation ability than PHI.

The baseline spectra were the same as the CH₃SH Abs. 30 min spectral curve in Fig. 9a when the photodegradation experiment performed. It was found that the peak intensity of the corresponding CH₃SH at 806, 1455 cm⁻¹ decreased with the reaction [55], while the signal intensity of the oxidation products increased significantly (Fig. 9b), implying that the CH₃SH adsorbed on the PHI surface was gradually consumed under photocatalytic conditions. The intensity of the corresponding peaks in Cu (111)/PHI system decreased more rapidly (Fig. 9d). Specifically, the peaks at 752 cm⁻¹, 822 cm⁻¹, and 2926 cm⁻¹ gradually decreased in intensity, indicating that the S elements in

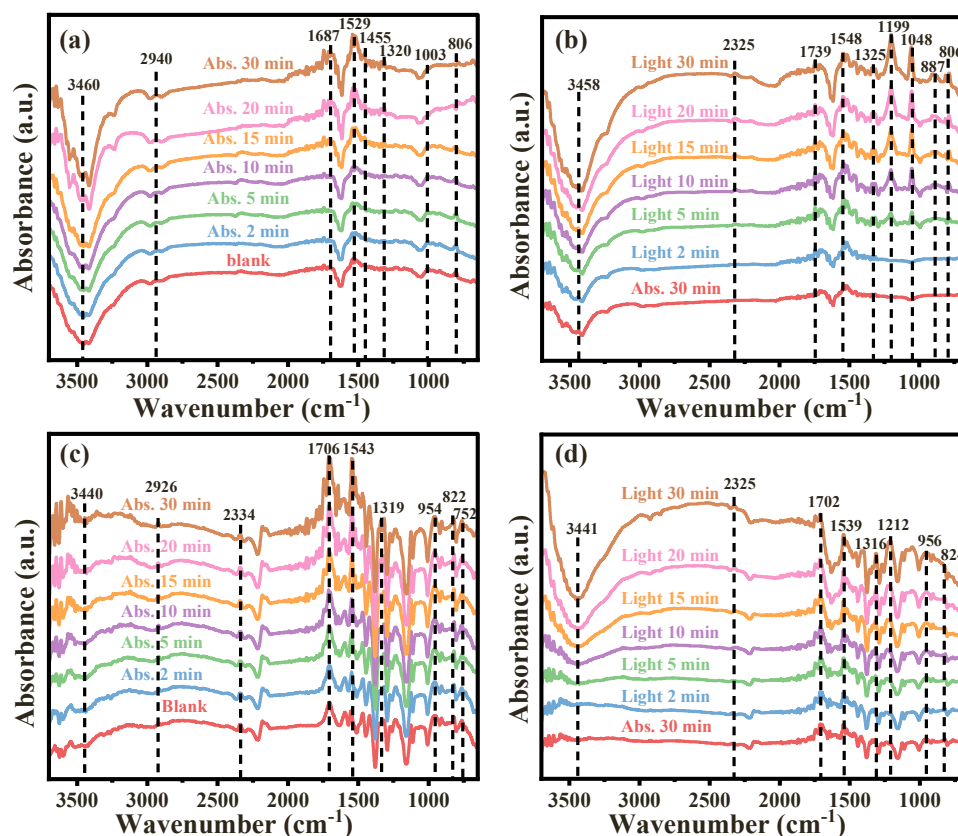


Fig. 9. In situ DRIFTS spectra of (a, c) adsorption and (b, d) photocatalytic removal for CH_3SH with PHI and Cu (111)/PHI. The IR spectrum was collected with interval times of 0 min, 2 min, 5 min, 10 min, 15 min, 20 min and 30 min.

CH_3SH are gradually oxidized. The emerging peak at 1212 cm^{-1} belongs to the $-\text{COO}$ groups in the bidentate carbonate. Compared with PHI, the peaks of CO_2 at 2325 cm^{-1} and H_2O at 3441 cm^{-1} increased more significantly in Cu (111)/PHI during the photocatalytic stage, which also indicated that Cu (111)/PHI had a stronger oxidation capacity and could effectively oxidize CH_3SH deeply to CO_2 and H_2O . In addition to trace CO_2 and H_2O production, PHI has more intermediate products on its surface: SO_3^{2-} (1048 cm^{-1}), CH_3SO_3^- (1199 cm^{-1}). The contact angle (CA) was tested to reveal the hydrophobic of catalyst, which served as a metric for evaluating the ability to expel the terminal/final hydrophilic substances. Results displayed in Fig. S15a and S15b, the surface of PHI exhibited extreme hydrophilicity and the CA steadily decreased from 13.02° to 9.31° as time increased from 0 s to 0.5 s, and its super-hydrophilic surface structure caused a series of hydrophilic products (H_2O , CO_3^{2-} , SO_4^{2-}) to gradually accumulate on the surface to the extent of masking its surface-active sites and further reduced its durability. In contrast, the CA of Cu (111)/PHI (71.35°) exhibited lower hydrophilicity, while the CA was still 63.45° when the residence time extended to 0.5 s (Fig. S15c and S15d). This result reflected that the coupling Cu (111) with PHI enhanced the catalyst's surface hydrophobic, which would facilitate the rapid transfer of hydrophilic products away from the surface. The surface hydrophilicity of Cu (111)/PHI slightly increased after reaction, and CA decreased from 46.85° to 34.86° (Fig. S15e and S15f), but it was still superior to that of pure PHI. Therefore, the introduction of Cu (111) as an electron pump for rapid transfer of electrons, and enhanced the surface hydrophobicity of the carrier catalysts is an effective strategy to improve the resistance to coking and durability of the catalysts.

3.5. Theoretical calculations

Density functional theory (DFT) calculations was used to investigate

the catalytic mechanism at the molecular level [56]. The optimized geometries of small molecules (Fig. S16 and Table S4), PHI (Fig. S17), and Cu (111)/PHI (Fig. S18) were prepared. As presented in Fig. 10 a-f, the adsorption energies (E_{ads}) of small molecules on PHI and Cu (111)/PHI were all negative, demonstrating that the adsorption of molecules was energetically favorable. Specifically, the E_{ads} of O_2 , CH_3SH , and H_2O on Cu (111)/PHI were -1.50 eV , -0.683 eV , and -0.371 eV (Fig. 10 d-f), which higher than E_{ads} of O_2 (-0.206 eV), H_2O (-0.109 eV), and CH_3SH (-0.097 eV) on PHI (Fig. 10 a-c). The results indicated that the adsorption ability of Cu (111)/PHI was significantly stronger than that of PHI. The O-O bond length slightly increased from 1.236 \AA to 1.258 \AA after O_2 adsorption on PHI, while O-O bond length increased to 1.367 \AA after O_2 adsorption on Cu (111)/PHI, the (Table S5). Additionally, the ability of adsorption and activation showed similar results for H_2O and CH_3SH as well, indicating that Cu (111)/PHI were more favorable for the adsorption and activation of H_2O and O_2 molecules, thus facilitating the generation of ROS [57]. The charge density difference (CDD) was illustrated in Figs. 10g and 10h and the apparent charge depletion was found near PHI region ($2.5\text{--}4.2\text{ \AA}$) and electron enriches on the surface of Cu (111) ($4.5\text{--}5.5\text{ \AA}$) and CH_3SH ($6.3\text{--}7.0\text{ \AA}$), which illustrated that the photogenerated electrons were transferred from PHI to CH_3SH , and Cu (111) nanocrystal acted as external electron pump [58]. The Bader charge distributions revealed that elements C and N tended to lose electrons to form of a positive ion region [59] in both the PHI and Cu (111)/PHI systems (Fig. S19a and S19b). Due to the significantly enhanced electron pump effect of Cu (111) nanocrystal, the formed and strengthen built-in electric field inside Cu (111)/PHI promoted more photogenerated electrons to migrate to the surface of Cu (111) nanocrystals (1.34 e) and generated a stronger electronic interaction with CH_3SH molecules (0.35 e) [60], the obtained of electrons for CH_3SH naturally led to the formation of CH_3S^- . However, PHI excited only a small number of photogenerated electrons,

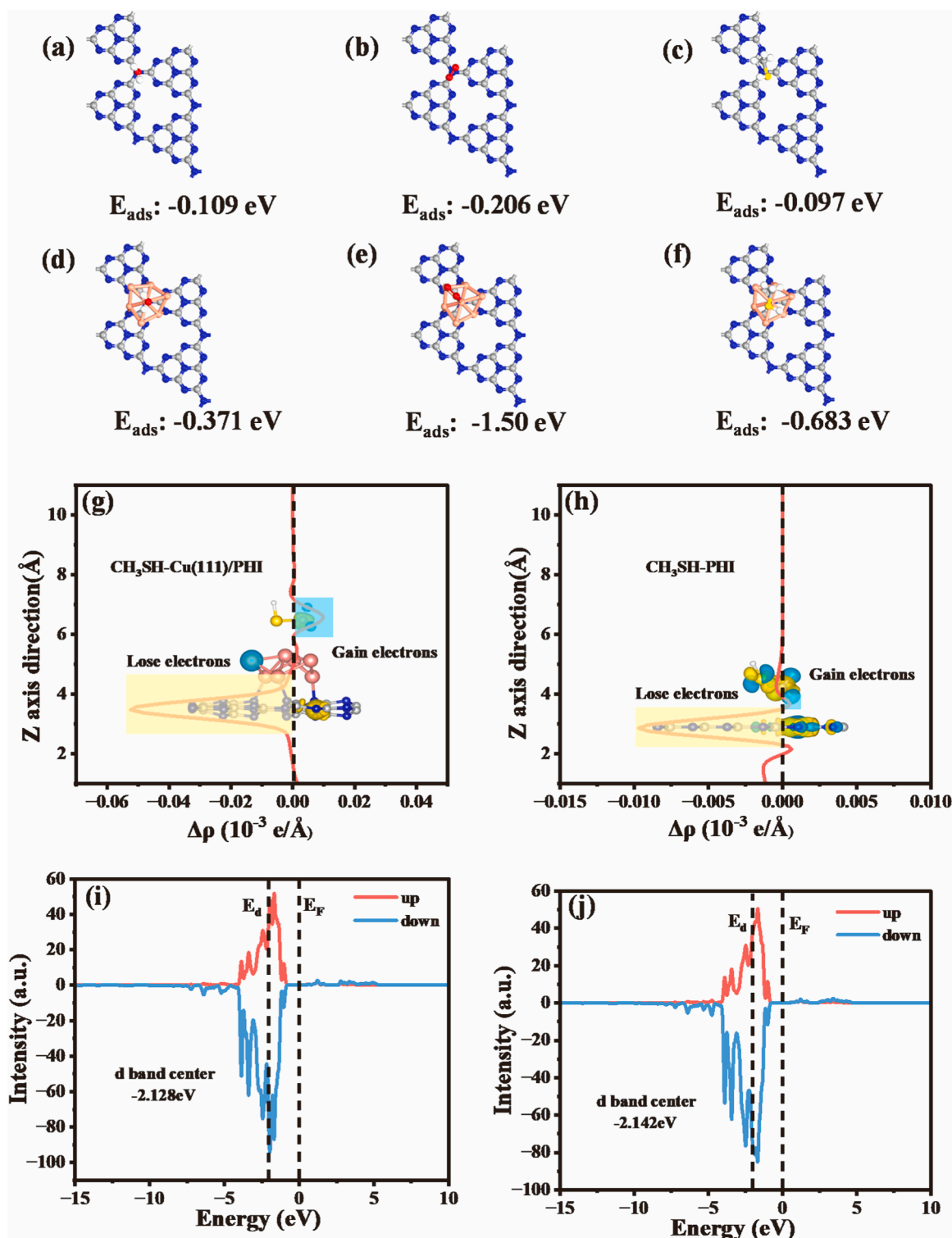


Fig. 10. Adsorption energy of (a) H₂O, (b) O₂ and (c) CH₃SH over the PHI; Adsorption energy of (d) H₂O, (e) O₂ and (f) CH₃SH over the Cu (111)/PHI; The charge density difference of (g) CH₃SH-Cu (111)/PHI system and (h) CH₃SH-PHI system (yellow and cyan regions represent charge depletion and charge accumulation); The d-band centers of Cu elements in (i) Cu (111)/PHI system and (j) CH₃SH-Cu (111)/PHI system.

which made weak electronic interaction with CH₃SH molecules (0.24 e). In words, Cu (111) nanocrystals can more easily extract the excited photogenerated electrons from PHI and rapidly deliver to the adsorbed CH₃SH molecules for generate initial products (CH₃S[•]).

Nørskov's d-band theory provides a semi-quantitative explanation of the binding of small molecules on transition metal surfaces and places the physical concept in chemical language [61]. Projected partial

density of states (PDOS) was used to analysis d-band of Cu atoms in Cu (111)/PHI before and after CH₃SH absorption. In Figs. 10i and 10j, the asymmetric peak confirmed the presence of unpaired electrons in the outermost d orbitals of Cu atoms [15], which facilitated the enhancement of the hybridization between the d orbitals of Cu atoms and the P orbitals of adsorbed small molecules, and facilitates the adsorption of small molecules. The lower d-band center of Cu atoms in Cu (111)/PHI

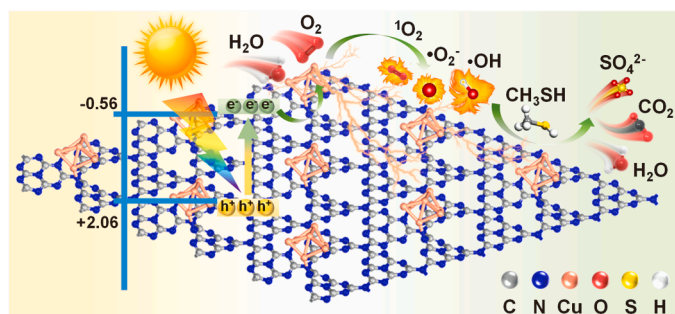
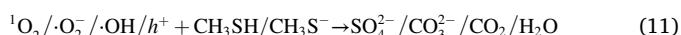


Fig. 11. The possible mechanism diagram of Cu (111)/PHI for photocatalytic CH₃SH elimination.

($E_d = -2.128$ eV) meant the anti-bonding state of Cu-N filling with fewer electrons, thereby enhancing the adsorption of molecule on the Cu site. After CH₃SH adsorbed, the d-band center of Cu atoms shifted downward to $E_d = -2.142$ eV, accompanied by a reduction in the number of electrons, indicating electrons transferred from Cu (111) to CH₃SH. The efficient adsorption of CH₃SH on catalyst surface was important for further smoothly oxidation, and the lower d-band center will increase the filling of as-hybridized antibonding orbitals ((d-σ)^{*}) to disrupt the interaction between CH₃SH and Cu (111)/PHI, thus thermodynamically enhancing electronic interactions between them [62], which eventually enhanced the performance of photocatalytic CH₃SH elimination. The reaction process of CH₃SH elimination is described as follows equations:



4. Conclusions

In conclusion, we constructed a novel photocatalyst by coupling Cu (111) nanocrystals and heptazine PHI for greatly enhancing carrier mobility and facilitating photocatalytic elimination of CH₃SH. Cu (111)/PHI showed excellent CH₃SH elimination performance of 87.8% per 30 min, which was 1.22, 1.24 times higher than Cu (100)/PHI, Cu (111 + 100)/PHI and was superior than the other reported CH₃SH elimination technologies. By combining activity evaluation, In-situ XPS, In-situ DRIFTS, fs-TAS, EPR characterizations, the photocatalytic improvement is demonstrated to be due to the enhanced electron pump effect of Cu (111) nanocrystals and efficiently activated H₂O, O₂ molecule, Cu (100)/PHI and Cu (111 + 100)/PHI. And DFT calculations further showed that the performance enhancement was mainly ascribe to the d-band unpaired electrons of Cu (111) nanocrystal regulated the adsorption strength of small molecules and promoted their activation, thus achieving efficient photocatalytic activity. This research will provide some inspiration for future design of photocatalysts for effective electron transfer based on facet engineering and provide an

understanding of the interfacial microenvironment of photocatalysts through a combination of fs-TAS tests and experimental measurements.

CRediT authorship contribution statement

Tao Zhong: Methodology, Validation, Computation, Investigation, Data curation, Writing – original draft, Visualization. **Su Tang, Wenbin Huang:** Data curation, Visualization, Software. **Wei Liu:** Data curation, Formal analysis. **Huinan Zhao, Lingling Hu:** Writing – review & editing, Methodology, Validation, Investigation, Data curation, Software. **Shuanghong Tian, Chun He:** Conceptualization, Supervision, Funding acquisition, Writing – review & editing.

Declaration of Competing Interest

The authors declare that they have no known competing financial interests or personal relationships that could have appeared to influence the work reported in this paper.

Data availability

Data will be made available on request.

Acknowledgments

The authors thank the National Natural Science Foundation of China (Nos. 52070195, 21876212), Guangdong Basic and Applied Basic Research Foundation (No. 2023A1515012198) for financially supporting this work.

Appendix A. Supporting information

Supplementary data associated with this article can be found in the online version at doi:10.1016/j.apcatb.2023.123476.

References

- [1] G. Zhu, W. Zhu, Y. Lou, J. Ma, W. Yao, R. Zong, Y. Zhu, Encapsulate α-MnO₂ nanofiber within graphene layer to tune surface electronic structure for efficient ozone decomposition, *Nat. Commun.* 12 (2021) 4152, [10.1038/s41467-021-24424-x](https://doi.org/10.1038/s41467-021-24424-x).
- [2] J. Wang, Y. Ding, Q. Dai, W. Zhang, Z. Jiang, Y. Qu, C. Kong, Z. Yang, T. Wang, H. Zhu, One-step hydrothermal synthesis of Bi₂W₂Mo_{1-x}O₆ solid solution with adjustable energy band coupling with g-C₃N₄: 2D/2D Z-scheme heterojunction for enhanced photocatalytic HCHO degradation under indoor conditions, *Sep. Purif. Technol.* 314 (2023), 123551, <https://doi.org/10.1016/j.seppur.2023.123551>.
- [3] Z. Wang, Q. Wei, N. Zhang, X. Shi, M. Chen, Y. Huang, J. Cao, H. Li, W. Ho, S. Lee, Simultaneous polarization engineering and selectivity regulation achieved using polymeric carbon nitride for promoting NO_x photo-oxidation, *Appl. Catal. B: Environ.* 330 (2023), 122582, <https://doi.org/10.1016/j.apcatb.2023.122582>.
- [4] Y. Guo, M. Wen, G. Li, T. An, Recent advances in VOC elimination by catalytic oxidation technology onto various nanoparticles catalysts: a critical review, *Appl. Catal. B: Environ.* 281 (2021), 119447, <https://doi.org/10.1016/j.apcatb.2020.119447>.
- [5] L.-Y. Lin, C. Liu, V. Dien Dang, H.-T. Fu, Atomically dispersed Ti-O clusters anchored on NH₂-UiO-66(Zr) as efficient and deactivation-resistant photocatalyst for abatement of gaseous toluene under visible light, *J. Colloid Interface Sci.* 635 (2023) 323–335, <https://doi.org/10.1016/j.jcis.2022.12.147>.
- [6] M. Liu, C. Wei, H. Zhuzhang, J. Zhou, Z. Pan, W. Lin, Z. Yu, G. Zhang, X. Wang, Fully condensed poly (Triazine Imide) crystals: extended π-conjugation and structural defects for overall water splitting, *Angew. Chem. Int. Ed.* 61 (2022), e202113389, <https://doi.org/10.1002/anie.202113389>.
- [7] H. Che, P. Wang, J. Chen, X. Gao, B. Liu, Y. Ao, Rational design of donor-acceptor conjugated polymers with high performance on peroxydisulfate activation for pollutants degradation, *Appl. Catal. B: Environ.* 316 (2022), 121611, <https://doi.org/10.1016/j.apcatb.2022.121611>.
- [8] F. Guo, B. Hu, C. Yang, J. Zhang, Y. Hou, X. Wang, On-surface polymerization of in-plane highly ordered carbon nitride nanosheets toward photocatalytic mineralization of mercaptan gas, *Adv. Mater.* 33 (2021) 2101466, <https://doi.org/10.1002/adma.202101466>.
- [9] H.-L. Wu, R. Sato, A. Yamaguchi, M. Kimura, M. Haruta, H. Kurata, T. Teranishi, Formation of pseudomorphic nanocages from Cu₂O nanocrystals through anion exchange reactions, *Science* 351 (2016) 1306–1310, <https://doi.org/10.1126/science.125520>.

- [10] M. Monai, K. Jenkinson, A.E.M. Melcherts, J.N. Louwen, E.A. Irmak, S. Van Aert, T. Altantzis, C. Vogt, W. van der Stam, T. Duchon, B. Šmíd, E. Groeneveld, P. Berben, S. Bals, B.M. Weckhuysen, Restructuring of titanium oxide overlayers over nickel nanoparticles during catalysis, *Science* 380 (2023) 644–651, <https://doi.org/10.1126/science.adf6984>.
- [11] W. He, J. Zhang, S. Dieckhöfer, S. Varhade, A.C. Brix, A. Lielpetere, S. Seisel, J.R.C. Junqueira, W. Schuhmann, Splicing the active phases of copper/cobalt-based catalysts achieves high-rate tandem electroreduction of nitrate to ammonia, *Nat. Commun.* 13 (2022) 1129, [10.1038/s41467-022-28728-4](https://doi.org/10.1038/s41467-022-28728-4).
- [12] T. Zhong, Z. Yu, R. Jiang, J. Huang, Y. Hou, J. Chen, Y. Zhang, H. Zhu, B. Wang, L. Ding, Activation strategy of WS₂ as an efficient photocatalytic hydrogen evolution cocatalyst through Co²⁺ doping to adjust the highly exposed active (100) facet, *Sol. RRL* 5 (2021) 2100223, <https://doi.org/10.1002/solr.202100223>.
- [13] J. Qin, L. Chen, K. Wu, X. Wang, Q. Zhao, L. Li, B. Liu, Z. Ye, Electrochemical synthesis of ammonium from nitrates via surface engineering in Cu₂O (100) facets, *ACS Appl. Energy Mater.* 5 (2022) 71–76, <https://doi.org/10.1021/acsaem.1c02319>.
- [14] Z.-Z. Wu, X.-L. Zhang, Z.-Z. Niu, F.-Y. Gao, P.-P. Yang, L.-P. Chi, L. Shi, W.-S. Wei, R. Liu, Z. Chen, S. Hu, X. Zheng, M.-R. Gao, Identification of Cu(100)/Cu(111) interfaces as superior active sites for CO dimerization during CO₂ electroreduction, *J. Am. Chem. Soc.* 144 (2022) 259–269, <https://doi.org/10.1021/jacs.1c09508>.
- [15] J. Wang, Y.-C. Huang, Y. Wang, H. Deng, Y. Shi, D. Wei, M. Li, C.-L. Dong, H. Jin, S. S. Mao, S. Shen, Atomically dispersed metal-nitrogen-carbon catalysts with d-orbital electronic configuration-dependent selectivity for electrochemical CO₂-to-CO reduction, *ACS Catal.* 13 (2023) 2374–2385, <https://doi.org/10.1021/acscatal.2c05249>.
- [16] W. Qu, Z. Tang, W. Liu, Y. Liao, Y. Huang, D. Xia, Q. Lian, S. Tian, C. He, D. Shu, Self-accelerating interfacial catalytic elimination of gaseous sulfur-containing volatile organic compounds as microbubbles in a facet-engineered three-dimensional BiOCl sponge fenton-like process, *Environ. Sci. Technol.* 56 (2022) 11657–11669, <https://doi.org/10.1021/acs.est.2c01798>.
- [17] H. Chen, H. Li, S. Chen, L. Sheng, Z. Zhang, W. Wu, M. Fan, L. Wang, B. Yang, Atomic Pd dispersion in triangular Cu nanosheets with dominant (111) plane as a tandem catalyst for highly efficient and selective electrodehalogenation, *Appl. Catal. B: Environ.* 328 (2023), 122480, <https://doi.org/10.1016/j.apcatb.2023.122480>.
- [18] T. Zhao, J. Li, J. Liu, F. Liu, K. Xu, M. Yu, W. Xu, F. Cheng, Tailoring the catalytic microenvironment of Cu₂O with SiO₂ to enhance C₂ product selectivity in CO₂ electroreduction, *ACS Catal.* 13 (2023) 4444–4453, <https://doi.org/10.1021/acscatal.3c00056>.
- [19] S. Sun, J. Li, H. Ding, B. Zhang, H. Huang, Z. Xu, Y. Tu, D. Chen, X. Duan, Engineered tourmaline/g-C₃N₄ composites for photocatalytic Fenton-like oxidation: synergy of spontaneous interface polarization and surface iron circulations induced by minerals, *Chem. Eng. J.* 460 (2023), 141718, <https://doi.org/10.1016/j.cej.2023.141718>.
- [20] X. Wu, Q. Zhao, J. Zhang, S. Li, H. Liu, K. Liu, Y. Li, D. Kong, H. Sun, M. Wu, OD carbon dots intercalated Z-scheme CuO/g-C₃N₄ heterojunction with dual charge transfer pathways for synergistic visible-light-driven photo-Fenton-like catalysis, *J. Colloid Interface Sci.* 634 (2023) 972–982, <https://doi.org/10.1016/j.jcis.2022.12.052>.
- [21] L. Lin, Z. Lin, J. Zhang, X. Cai, W. Lin, Z. Yu, X. Wang, Molecular-level insights on the reactive facet of carbon nitride single crystals photocatalysing overall water splitting, *Nat. Catal.* 3 (2020) 649–655, <https://doi.org/10.1038/s41929-020-0476-3>.
- [22] L. Xu, L. Li, Z. Hu, J.C. Yu, EDTA-enhanced photocatalytic oxygen reduction on K-doped g-C₃N₄ with N-vacancies for efficient non-sacrificial H₂O₂ synthesis, *J. Catal.* 418 (2023) 300–311, <https://doi.org/10.1016/j.jcat.2023.01.019>.
- [23] X. Zheng, P. Yu, Y. Liu, Y. Ma, Y. Cao, Z. Cai, L. Zhou, K. Huang, S. Zheng, L. Jiang, Efficient hydrogenation of methyl palmitate to hexadecanol over Cu/m-ZrO₂ catalysts: synergistic effect of Cu species and oxygen vacancies, *ACS Catal.* 13 (2023) 2047–2060, <https://doi.org/10.1021/acscatal.2c06151>.
- [24] G. Ma, O.A. Syzgantseva, Y. Huang, D. Stoian, J. Zhang, S. Yang, W. Luo, M. Jiang, S. Li, C. Chen, M.A. Syzgantseva, S. Yan, N. Chen, L. Peng, J. Li, B. Han, A hydrophobic Cu/Cu₂O sheet catalyst for selective electroreduction of CO to ethanol, *Nature, Communications* 14 (2023) 501, [10.1038/s41467-023-36261-1](https://doi.org/10.1038/s41467-023-36261-1).
- [25] C. Liu, X.-D. Zhang, J.-M. Huang, M.-X. Guan, M. Xu, Z.-Y. Gu, In situ reconstruction of Cu-N coordinated MOFs to generate dispersive Cu/Cu₂O nanoclusters for selective electroreduction of CO₂ to C₂H₄, *ACS Catal.* 12 (2022) 15230–15240, <https://doi.org/10.1021/acscatal.2c04275>.
- [26] J.N. Burrow, R.A. Ciufio, L.A. Smith, Y. Wang, D.C. Calabro, G. Henkelman, C. B. Mullins, Calcium poly(heptazine imide): a covalent heptazine framework for selective CO₂ adsorption, *ACS Nano* 16 (2022) 5393–5403, <https://doi.org/10.1021/acsnano.1c08912>.
- [27] Y. Liu, H. Tan, Y. Wei, M. Liu, J. Hong, W. Gao, S. Zhao, S. Zhang, S. Guo, Cu₂O/2D COFs core/shell nanocubes with antiphotocorrosion ability for efficient photocatalytic hydrogen evolution, *ACS Nano* 17 (2023) 5994–6001, <https://doi.org/10.1021/acsnano.3c00358>.
- [28] P. Chen, B. Lei, X. Dong, H. Wang, J. Sheng, W. Cui, J. Li, Y. Sun, Z. Wang, F. Dong, Rare-earth single-atom La-N charge-transfer bridge on carbon nitride for highly efficient and selective photocatalytic CO₂ reduction, *ACS Nano* 14 (2020) 15841–15852, <https://doi.org/10.1021/acsnano.0c07083>.
- [29] Z. Li, Y. Chen, Simultaneously improving O₂ adsorption and activation for H₂O₂ photogeneration on K-doped-carbon nitride, *Chem. Commun.* 58 (2022) 13983–13986, <https://doi.org/10.1039/D2CC05898G>.
- [30] W. Xu, S. Zhang, R. Shen, Z. Peng, B. Liu, J. Li, Z. Zhang, B. Li, A catalytic copper/cobalt oxide interface for efficient hydrogen generation, *Energy Environ. Mater.* 6 (2023), e12279, <https://doi.org/10.1002/eeem2.12279>.
- [31] Z. Cui, S. Song, H. Liu, Y. Zhang, F. Gao, T. Ding, Y. Tian, X. Fan, X. Li, Synergistic effect of Cu⁺ single atoms and Cu nanoparticles supported on alumina boosting water-gas shift reaction, *Appl. Catal. B: Environ.* 313 (2022), 121468, <https://doi.org/10.1016/j.apcatb.2022.121468>.
- [32] S. Lu, J. Zhang, H. Meng, X. Qin, J. Huang, Y. Liang, F.-S. Xiao, Catalytic direct dehydrogenation of ethyl lactate to produce ethyl pyruvate over a synergetic Cu⁰/Cu⁺ interface, *Appl. Catal. B: Environ.* 325 (2023), 122329, <https://doi.org/10.1016/j.apcatb.2022.122329>.
- [33] C. Wang, H. Dai, L. Liang, N. Li, X. Cui, B. Yan, G. Chen, Enhanced mechanism of copper doping in magnetic biochar for peroxymonosulfate activation and sulfamethoxazole degradation, *J. Hazard. Mater.* 458 (2023), 132002, <https://doi.org/10.1016/j.jhazmat.2023.132002>.
- [34] W. Qu, Z. Tang, S. Tang, H. Wen, J. Fang, Q. Lian, D. Shu, C. He, Cation substitution induced d-band center modulation on cobalt-based spinel oxides for catalytic ozonation, *Adv. Funct. Mater.*, N/a (2023) 2301677, <https://doi.org/10.1002/adfm.202301677>.
- [35] W. Chen, Z. Wang, M. Tian, G. Hong, Y. Wu, M. Sui, M. Chen, J. An, F. Song, X. Peng, Integration of TADF photosensitizer as “Electron Pump” and BSA as “Electron Reservoir” for boosting type I photodynamic therapy, *J. Am. Chem. Soc.* 145 (2023) 8130–8140, <https://doi.org/10.1021/jacs.3c01042>.
- [36] J. Zhang, X. Liang, C. Zhang, L. Lin, W. Xing, Z. Yu, G. Zhang, X. Wang, Improved charge separation in poly(heptazine-triazine) imides with semi-coherent interfaces for photocatalytic hydrogen evolution, *Angew. Chem. Int. Ed.* 61 (2022), e202210849, <https://doi.org/10.1002/anie.202210849>.
- [37] D. Wang, J. Chen, X. Gao, Y. Ao, P. Wang, Maximizing the utilization of photo-generated electrons and holes of g-C₃N₄ photocatalyst for harmful algae inactivation, *Chem. Eng. J.* 431 (2022), 134105, <https://doi.org/10.1016/j.cej.2021.134105>.
- [38] T. Zhong, Z. Yu, R. Jiang, Y. Hou, H. Chen, L. Ding, C. Lian, B. Zou, Surface-activated Ti₃C₂T_x MXene cocatalyst assembled with CdZnS-formed OD/2D CdZnS/Ti₃C₂A40 Schottky heterojunction for enhanced photocatalytic hydrogen evolution, *Sol. RRL* 6 (2022) 2100863, <https://doi.org/10.1002/solr.202100863>.
- [39] Q. Zhang, J. Chen, X. Gao, H. Che, P. Wang, Y. Ao, In-depth insight into the mechanism on photocatalytic synergistic removal of antibiotics and Cr (VI): the decisive effect of antibiotic molecular structure, *Appl. Catal. B: Environ.* 313 (2022), 121443, <https://doi.org/10.1016/j.apcatb.2022.121443>.
- [40] C. Cui, X. Zhao, X. Su, N. Xi, X. Wang, X. Yu, X.L. Zhang, H. Liu, Y. Sang, Porphyrin-based donor-acceptor covalent organic polymer/ZnIn₂S₄ Z-scheme heterostructure for efficient photocatalytic hydrogen evolution, *Adv. Funct. Mater.* 32 (2022) 2208962, <https://doi.org/10.1002/adfm.202208962>.
- [41] F. Xue, Y. Si, C. Cheng, W. Fu, X. Chen, S. Shen, L. Wang, M. Liu, Electron transfer via homogeneous phosphorus bridges enabling boosted photocatalytic generation of H₂ and H₂O₂ from pure water with stoichiometric ratio, *Nano Energy* 103 (2022), 107799, <https://doi.org/10.1016/j.nanoen.2022.107799>.
- [42] J. Wu, Z. Liu, X. Lin, E. Jiang, S. Zhang, P. Huo, Y. Yan, P. Zhou, Y. Yan, Breaking through water-splitting bottlenecks over carbon nitride with fluorination, *Nature, Communications* 13 (2022) 6999, [10.1038/s41467-022-34848-8](https://doi.org/10.1038/s41467-022-34848-8).
- [43] P. Xia, X. Pan, S. Jiang, J. Yu, B. He, P.M. Ismail, W. Bai, J. Yang, L. Yang, H. Zhang, M. Cheng, H. Li, Q. Zhang, C. Xiao, Y. Xie, Designing a redox heterojunction for photocatalytic “Overall Nitrogen Fixation” under mild conditions, *Adv. Mater.* 34 (2022) 2200563, <https://doi.org/10.1002/adma.202200563>.
- [44] W. Wang, L. Du, R. Xia, R. Liang, T. Zhou, H.K. Lee, Z. Yan, H. Luo, C. Shang, D. L. Phillips, Z. Guo, In situ protonated-phosphorus interstitial doping induces long-lived shallow charge trapping in porous C_{3-x}N₄ photocatalysts for highly efficient H₂ generation, *Energy Environ. Sci.* 16 (2023) 460–472, <https://doi.org/10.1039/D2EE02680E>.
- [45] S. Zhang, H. Li, L. Wang, J. Liu, G. Liang, K. Davey, J. Ran, S.-Z. Qiao, Boosted photoreforming of plastic waste via defect-rich NiP₃ nanosheets, *J. Am. Chem. Soc.* 145 (2023) 6410–6419, <https://doi.org/10.1021/jacs.2c13590>.
- [46] W. Yang, R. Godin, H. Kasap, B. Moss, Y. Dong, S.A.J. Hillman, L. Steier, E. Reisner, J.R. Durrant, Electron accumulation induces efficiency bottleneck for hydrogen production in carbon nitride photocatalysts, *J. Am. Chem. Soc.* 141 (2019) 11219–11229, <https://doi.org/10.1021/jacs.9b04556>.
- [47] D. Gao, P. Deng, J. Zhang, L. Zhang, X. Wang, H. Yu, J. Yu, Reversing free-electron transfer of MoS_{2-x} cocatalyst for optimizing antibonding-orbital occupancy enables high photocatalytic H₂ evolution, *Angew. Chem. Int. Ed.* 62 (2023), e202304559, <https://doi.org/10.1002/anie.202304559>.
- [48] B. He, Z. Wang, P. Xiao, T. Chen, J. Yu, L. Zhang, Cooperative coupling of H₂O₂ production and organic synthesis over a floatable polystyrene-sphere-supported TiO₂/Bi₂O₃ S-scheme photocatalyst, *Adv. Mater.* 34 (2022) 2203225, <https://doi.org/10.1002/adma.202203225>.
- [49] Y. Wang, M. Liu, F. Fan, G. Li, J. Duan, Y. Li, G. Jiang, W. Yao, Enhanced full-spectrum photocatalytic activity of 3D carbon-coated C₃N₄ nanowires via giant interfacial electric field, *Appl. Catal. B: Environ.* 318 (2022), 121829, <https://doi.org/10.1016/j.apcatb.2022.121829>.
- [50] Y. Li, L. Wang, F. Zhang, W. Zhang, G. Shao, P. Zhang, Detecting and quantifying wavelength-dependent electrons transfer in heterostructure catalyst via in situ irradiation XPS, *Adv. Sci.* 10 (2023) 2205020, <https://doi.org/10.1002/advs.202205020>.
- [51] Q.-M. Sun, J.-J. Xu, F.-F. Tao, W. Ye, C. Zhou, J.-H. He, J.-M. Lu, Boosted inner surface charge transfer in perovskite nanodots/mesoporous titania frameworks for

- efficient and selective photocatalytic CO₂ reduction to methane, *Angew. Chem. Int. Ed.* 61 (2022), e202200872, <https://doi.org/10.1002/anie.202200872>.
- [52] H. Wang, Y. Sun, F. Dong, Insight into the Overlooked photochemical decomposition of atmospheric surface nitrates triggered by visible light, *Angew. Chem. Int. Ed.* 61 (2022), e202209201, <https://doi.org/10.1002/anie.202209201>.
- [53] W. Qu, Z. Tang, H. Wen, M. Luo, T. Zhong, Q. Lian, L. Hu, S. Tian, C. He, D. Shu, Electron transfer trade-offs in MOF-derived cobalt-embedded nitrogen-doped carbon nanotubes boost catalytic ozonation for gaseous sulfur-containing VOC elimination, *ACS Catal.* 13 (2023) 692–705, <https://doi.org/10.1021/acscatal.2c05285>.
- [54] H. Wen, W. Qu, M. Lin, L. Zhou, X. Guo, P. Ma, T. Wu, H. Zhao, T. Zhong, C. He, Nitrogen-coordinated cobalt embedded in hollow carbon polyhedron for catalytic ozonation of odor CH₃SH at ambient temperature, *Chem. Eng. J.* 471 (2023), 144567, <https://doi.org/10.1016/j.cej.2023.144567>.
- [55] C. He, Y. Wang, Z. Li, Y. Huang, Y. Liao, D. Xia, S. Lee, Facet engineered α -MnO₂ for efficient catalytic ozonation of odor CH₃SH: Oxygen vacancy-induced active centers and catalytic mechanism, *Environ. Sci. Technol.* 54 (2020) 12771–12783, <https://doi.org/10.1021/acs.est.0c05235>.
- [56] X. Shao, M. Liang, M.G. Kim, S. Ajmal, A. Kumar, X. Liu, H.S. Jung, H. Jin, F. Cao, J. Yu, K.M. Tran, H. Ko, J. Lee, J.W. Bae, H. Lee, Density-controlled metal nanocluster with modulated surface for pH-universal and robust water splitting, *Adv. Funct. Mater.* 33 (2023) 2211192, <https://doi.org/10.1002/adfm.202211192>.
- [57] Y. Lu, H. Deng, T. Pan, X. Liao, C. Zhang, H. He, Effective toluene ozonation over δ -MnO₂: Oxygen vacancy-induced reactive oxygen species, *Environ. Sci. Technol.* 57 (2023) 2918–2927, <https://doi.org/10.1021/acs.est.2c07661>.
- [58] F. Chen, J. Ding, K. Guo, L. Yang, Z. Zhang, Q. Yang, Y. Yang, Z. Bao, Y. He, Q. Ren, CoNi alloy nanoparticles embedded in metal-organic framework-derived carbon for the highly efficient separation of xenon and krypton via a charge-transfer effect, *Angew. Chem. Int. Ed.* 60 (2021) 2431–2438, <https://doi.org/10.1002/anie.202011778>.
- [59] L. Hu, R. Gao, A. Zhang, R. Yang, X. Zang, S. Wang, S. Yao, Z. Yang, H. Hao, Y.-M. Yan, Cu²⁺ intercalation activates bulk redox reactions of MnO₂ for enhancing capacitive performance, *Nano Energy* 74 (2020), 104891, <https://doi.org/10.1016/j.nanoen.2020.104891>.
- [60] Y.-H. Fan, Y.-W. Lu, F. Hayat, Y.-H. Mei, M. Chen, Overcoming slow removal efficiency-induced highly toxic I-DBPs in water by oxygen vacancies enriched invasive plant biochar catalyst: experimental and theoretical studies, *J. Hazard. Mater.* 459 (2023), 132086, <https://doi.org/10.1016/j.jhazmat.2023.132086>.
- [61] J.K. Nørskov, F. Abild-Pedersen, F. Studt, T. Bligaard, Density functional theory in surface chemistry and catalysis, *Proceedings of the National Academy of Sciences*, 108 (2011) 937–943. 10.1073/pnas.1006652108.
- [62] C. Rong, X. Shen, Y. Wang, L. Thomsen, T. Zhao, Y. Li, X. Lu, R. Amal, C. Zhao, Electronic structure engineering of single-stom Ru sites via Co-N₄ sites for bifunctional pH-universal water splitting, *Adv. Mater.* 34 (2022) 2110103, <https://doi.org/10.1002/adma.202110103>.